Ring modulator small-signal response analysis based on pole-zero representation

Samira Karimelahi* and Ali Sheikholeslami

Department of Electrical and Computer Engineering, University of Toronto, 10 King's College Road, Toronto, Ontario, M5S 3G4, Canada

*[*samira@ece.utoronto.ca](mailto:samira@ece.utoronto.ca)*

Abstract: We present a closed-form expression for the small-signal response of a depletion-mode ring modulator and verify it by measurement results. Both electrical and optical behavior of micro-ring modulator as well as the loss variation due to the index modulation is considered in the derivation. This expression suggests that a ring modulator is a third-order system with one real pole, one zero and a pair of complex-conjugate poles. The exact positions of the poles/zero are given and shown to be dependent upon parameters such as electrical bandwidth, coupling condition, optical loss, and sign/value of laser detunings. We show that the location of zero is different for positive and negative detuning, and therefore, the ring modulator frequency response is asymmetric. We use the gain-bandwidth product as a figure of merit and calculate it for various pole/zero locations. We show that gain-bandwidth for the over-coupled ring modulator is superior compared to other coupling conditions. Also, we show that the gain-bandwidth product can be increased to a limit by increasing the electrical bandwidth.

© 2016 Optical Society of America

OCIS codes: (130.4110) Modulators; (230.5750) Resonators; (250.0250) Optoelectronics.

References and links

1. G. Li, X. Zheng, J. Yao, H. Thacker, I. Shubin, Y. Luo, K. Raj, J. E. Cunningham, and A. V. Krishnamoorthy, "25Gb/s 1V-driving CMOS ring modulator with integrated thermal tuning," Opt. Express **19**(21), 20435–20443 (2011).
2. X. Zheng, F. Liu, J. Lexau, D. Patil, G. Li, Y. Luo, H. Thacker, I. Shubin, J. Yao, K. Raj, R. Ho, J. E. Cunningham, A. V. Krishnamoorthy, , "Ultralow power 80 Gb/s arrayed CMOS silicon photonic transceivers for WDM optical links," J Lightwave Technol. **30**(4), 641-650 (2012).
3. M. Pantouvaki, P. Verheyen, G. Lepage, J. De Coster, H. Yu, P. De Heyn, A. Masood, W. Bogaerts, P. Absil, and J. Van Campenhout, "8 × 14Gb/s Si ring WDM modulator array with integrated tungsten heaters and Ge monitor photodetectors," in *Optical Fiber Communications Conference and Exhibition* (OFC, 2014), pp. 1–3.
4. H. Li, Z. Xuan, A. Titriku, C. Li, K. Yu, B. Wang, A. Shafik, N. Qi, Y. Liu, R. Ding, "22.6 A 25Gb/s 4.4 V-swing AC-coupled Si-photonic microring transmitter with 2-tap asymmetric FFE and dynamic thermal tuning in 65nm CMOS," in *IEEE International Solid-State Circuits Conference* (ISSCC, 2015), pp. 1–3.
5. G. T. Reed, G. Mashanovich, F. Y. Gardes, and D. J. Thomson, "Silicon optical modulators," Nat. Photonics **4**(8), 518–526 (2010).
6. D. A. Miller, "Device requirements for optical interconnects to silicon chips," Proc. IEEE **97**(7), 1166–1185 (2009).
7. N. Ophir, C. Mineo, D. Mountain, and K. Bergman, "Silicon photonic microring links for high-bandwidth-density, low-power chip I/O," Micro. IEEE **33**, 54–67 (2013).

8. P. Dong, S. Liao, D. Feng, H. Liang, D. Zheng, R. Shafiiha, C. C. Kung, W. Qian, G. Li, X. Zheng, A. V. Krishnamoorthy, and M. Asghari, "Low V pp, ultralow-energy, compact, high-speed silicon electro-optic modulator," Opt. Express **17**(25), 22484–22490 (2009).
9. H. Yu, D. Ying, M. Pantouvaki, J. Van Campenhout, P. Absil, Y. Hao, J. Yang, and X. Jiang, "Trade-off between optical modulation amplitude and modulation bandwidth of silicon micro-ring modulators," Opt. Express **22**(12), 15178–15189 (2014).
10. J. Müller, F. Merget, S. S. Azadeh, J. Hauck, S. R. García, B. Shen, and J. Witzens, "Optical peaking enhancement in high-speed ring modulators," Sci. Rep. **4**,(2014).
11. Q. Xu, B. Schmidt, J. Shakya, and M. Lipson, "Cascaded silicon micro-ring modulators for WDM optical interconnection," Opt. Express **14**(20), 9431–9435(2006).
12. B. Pile and G. Taylor, "Small-signal analysis of microring resonator modulators," Opt. Express **22**, 14913–14928 (2014).
13. Y. Ban, J.-M. Lee, B.-M. Yu, S.-H. Cho, and W.-Y. Choi, "Small-signal frequency responses for si micro-ring modulators," in *Proceedings of IEEE Optical Interconnects Conference* (IEEE, 2014), pp. 47–48.
14. W. D. Sacher and J. K. Poon, "Dynamics of microring resonator modulators," Opt. Express **16**(20), 15741–15753 (2008).
15. J. Rhim, Y. Ban, B.-M. Yu, J.-M. Lee, and W.-Y. Choi, "Verilog-A behavioral model for resonance-modulated silicon micro-ring modulator," Opt. Express **23**(7), 8762–8772 (2015).
16. R. Dube-Demers, J. St-Yves, A. Bois, Q. Zhong, M. Caverley, Y. Wang, L. Chrostowski, S. LaRochelle, D. Plant, and W. Shi, "Analytical modeling of silicon microring and microdisk modulators with electrical and optical dynamics," J Lightwave Technol. **33**, 4240–4252 (2015).
17. S. Sharif Azadeh ; J. Mller ; F. Merget ; S. Romero-Garca ; B. Shen ; J. Witzens; "Advances in silicon photonics segmented electrode Mach-Zehnder modulators and peaking enhanced resonant devices," Proc. SPIE **9288**, 928817 (2014).
18. G. Ghione, *Semiconductor Devices for High-Speed Optoelectronics* (Cambridge, 2009), Ch. 6.
19. H. A. Haus, *Waves and Fields in Optoelectronics* (Prentice-Hall, 1984).
20. B. Little, S. Chu, H. Haus, J. Foresi, and J.-P. Laine, "Microring resonator channel dropping filters," J Lightwave Technol. **15**, 998–1005 (1997).
21. *http://www.ime.a-star.edu.sg/PPSSite/index.asp*.
22. W. R. McKinnon, D. X. Xu, C. Storey, E. Post, A. Densmore, A. Delâge, P. Waldron, J. H. Schmid, and S. Janz, "Extracting coupling and loss coefficientsfrom a ring resonator," Opt. Express **17**, 18971–18982 (2009).
23. T. Baehr-Jones, R. Ding, Y. Liu, A. Ayazi, T. Pinguet, N. C. Harris, M. Streshinsky, P. Lee, Y. Zhang, A. E.-J. Lim, T.-Y. Liow, S. H.-G. Teo, G.-Q. Lo, and M. Hochberg, "Ultralow drive voltage silicon traveling-wave modulator," Opt. Express **20**, 12014–12020 (2012).
24. T. Baehr-Jones, R. Ding, A. Ayazi, T. Pinguet, M. Streshinsky, N. Harris, J. Li, L. He, M. Gould, Y. Zhang, A. E.-J. Lim, T.-Y. Liow, S. H.-G. Teo, G.-Q. Lo, and M. Hochberg,, "A 25 Gb/s silicon photonics platform," arXiv preprint arXiv:1203.0767 (2012).

1. Introduction

Optical interconnects are the great candidate to replace the electrical interconnects in the short reach inter-chip and intra-chip communications. This is due to the fact that at high data rates, copper links become lossy. Among various candidates of optical modulators in silicon photonics links, carrier-depletion silicon ring modulators employing reverse-biased pn diode are the most favorable [1–4] due to their small footprints, high bandwidth, CMOS compatibility, low power consumption, and their suitability to wavelength division multiplexing (WDM) [5–7]. In order to optimally design carrier-depletion ring modulators in terms of power efficiency and bandwidth, it is essential to gain a better understanding of the device performance and its design trade-offs.

One of the most important performance metrics of a ring modulator is the small-signal electro-optical frequency response. It was shown recently that the widely used empirical formula relating the bandwidth of the ring modulator (f_{3dB}) to its optical (f_Q) and electrical (f_{RC}) bandwidths ($1/f_{3dB}^2 = 1/f_Q^2 + 1/f_{RC}^2$ [8]) is not accurate because it neglects the impact of other key parameters such as carrier wavelength and coupling condition [9, 10]. For example, when the input is detuned from the resonance wavelength, a peak may appear in the elector-optical response of the ring modulator before the roll-off. This effect has been shown to increase the bandwidth of the ring modulators [9–11].

Several studies on analyzing ring modulator small-signal frequency response were published recently based on experimental and/or numerical results [9, 10, 12–16] and the design tradeoffs of the ring modulator were investigated [9, 10, 12]. The bandwidth and DC modulation efficiency (DC gain) of the ring modulator were extracted from the small-signal response [9, 12, 13] as the important design parameters. However, a closed-form expression for electro-optical frequency response of a ring modulator considering both electrical and optical characteristics as well as the loss modulation accompanying the index modulation is missing to the best of our knowledge. Laser detuning has been optimized based on the DC gain previously [9, 10, 12], however, the widely used gain-bandwidth product (GBW) in electronics is a more appropriate figure of merit (FOM) for ring modulators. This is because it includes both ring modulator performance metrics of DC gain and bandwidth. GBW was considered in [17] as a FOM, but limited analysis was presented.

In this paper, we report a closed-form frequency response model of a carrier-depletion ring modulators. The model is verified by the measurement results. We show that for a non-zero detuning, the ring modulator electro-optical transfer function in the small-signal domain is a third-order system with one real pole, one zero, and a pair of complex-conjugate poles. This modeling allows us to assess the response of the ring modulator based on the pole/zero locations which depend on electrical bandwidth, coupling condition, optical loss, and laser detuning. Through such a modeling, we show that the asymmetric frequency response of the ring modulator arises from the different zero locations. At various pole/zero locations, GBW is found as a ring modulator performance metric where an optimum laser detuning is obtained based on the maximum GBW. An expression for f_{3dB} and GBW are also obtained for a critical coupling condition assuming large f_{RC}. We also assess the frequency response at zero detuning and show that it is coupling-condition dependent.

2. Small-signal modeling of a ring modulator

In this section, we aim to obtain a complete small-signal transfer function of a depletion mode intracavity modulated microring. Driving a ring modulator with the small sinusoidal voltage of $\widetilde{v_{in}}(t) = V_{in}\cos(\omega_m t)$ in addition to the DC voltage of V_{DC}, the input voltage, $v_{in}(t)$, can be written as $v_{in}(t) = V_{DC} + \mathrm{Re}(\hat{V}_{in}e^{j\omega_m t})$. Here, $\hat{V}_{in}$ is the small-signal phasor which is equal to amplitude of V_{in} and ω_m is modulation angular frequency. Under the small-signal assumptions, in response to this stimulus, the output optical power $P_{out}(t)$ oscillates at ω_m. The output power is equal to $P_{DC} + P_{out}\cos(\omega_m t + \phi_p) = P_{DC} + \mathrm{Re}(\hat{P}_{out}e^{j\omega_m t})$ where P_{DC} is the DC optical power, ϕ_p is the phase delay with respect to drive voltage, and $\hat{P}_{out}$ is a complex small-signal phasor. The total small-signal transfer function of a ring modulator, $H_t(\omega_m)$, is defined as [18]:

$$H_t(\omega_m) = \frac{\hat{P}_{out}}{\hat{V}_{in}}. \tag{1}$$

To obtain $H_t(\omega_m)$, the response of the ring modulator to a small-signal driving voltage can be divided into three parts of electrical ($H_E(\omega_m)$), electro-optical (H_{EO}), and optical ($H_O(\omega_m)$) responses as shown in Fig. 1. The small-signal equivalent circuit of a ring modulator [1] is shown in Fig. 1 and it includes C_{pad}, C_j, and C_{ox} as the capacitance between the pads through the top dielectrics, the capacitance of the reverse-biased pn junction, and the capacitance through the oxide layer, respectively. Also, R_{in}, R_j, and R_{Si} are the input resistor, the series resistance of the pn junction, and the resistance of the Si substrate. The electrical response of a ring modulator can be modeled as a low pass filter by its dominant pole as:

$$H_E(\omega_m) = \frac{1}{1 + j\omega_m R_{eq}C_{eq}}. \tag{2}$$

The filtered AC voltage across the pn junction (Fig. 1), $\widetilde{v}_j(t)$ is:

$$\widetilde{v}_j(t) = \hat{V}_{in} |H_E(\omega_m)| \cos(\omega_m t + \phi_{HE}(\omega_m)), \qquad (3)$$

where ϕ_{HE} is the phase delay caused by the electrical circuit model of a ring modulator.

As illustrated in Fig. 1, due to the voltage-dependent effective index and electric field decay time constant, both the resonance angular frequency, ω_r, and the shape of the ring modulator optical transmission spectrum are modulated. The effective index and the decay time constant modulations can be lumped together as $\widetilde{\omega}_r(t) = \Omega_r \cos(\omega_m t + \phi_{HE}(\omega_m))$, where Ω_r is a complex number equal to $\hat{V}_{in} \times |H_E(\omega_m)| \times H_{EO}$, and H_{EO} is:

$$H_{EO} = (\frac{-\omega_r}{n_g} \frac{\partial n_{eff}}{\partial v}\Big|_{V_{DC}} + j \frac{\partial(1/\tau)}{\partial v}\Big|_{V_{DC}}). \qquad (4)$$

Here, n_g is the group index, n_{eff} is the effective refractive index, and τ is the electric field amplitude decay time constant.
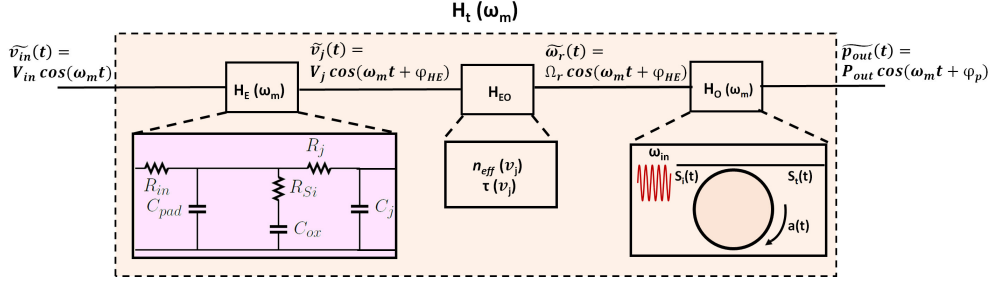

Fig. 1. Ring modulator small-signal block diagram.

So far, we have modeled H_E and H_{EO}. Instead of calculating the third transfer function (Fig. 1), H_O, we use the coupled mode theory [19,20] to first find $\hat{P}_{out}$ and subsequently $H_t(\omega_m)$. From coupled mode theory, the optical behavior of microring can be modeled using the following Eqs:

$$\frac{da}{dt} = (j\omega_r - \frac{1}{\tau})a - j\mu S_i, \qquad (5a)$$

$$S_t = S_i - j\mu a, \qquad (5b)$$

where a is the energy amplitude circulating inside the ring and $1/\tau = 1/\tau_e + 1/\tau_l$, with τ_l and τ_e being the amplitude decay time constants due to the intrinsic loss inside the cavity and due to the ring to bus waveguide coupling, respectively. Also, S_i and S_t are the CW input and time varying transmitted waves, and μ is the mutual coupling coefficient between the ring and the bus waveguide which is related to τ_e through $\mu^2 = 2/\tau_e$. In the steady state domain and for a harmonic input of $S_i = S_{i0}e^{j\omega_{in}t}$, where ω_{in} is the carrier angular frequency, a and S_t can be calculated from Eq. (5a) and (5b). Considering $a = a_0 e^{j\omega_{in}t}$ and $S_t = S_{t0}e^{j\omega_{in}t}$, we have:

$$a_0 = \frac{-j\mu}{j\Delta\omega + \frac{1}{\tau}} S_{i0}$$

$$S_{t0} = \frac{j\Delta\omega + \frac{1}{\tau} - \frac{2}{\tau_e}}{j\Delta\omega + \frac{1}{\tau}} S_{i0}, \qquad (6)$$

where $\Delta\omega = \omega_{in} - \omega_r$.

In the dynamic small-signal domain where we have $\omega_r + \widetilde{\omega_r}(t)$, the energy amplitude a will change by a small amount of δa. As shown in [10], first order perturbation theory can be used to find δa from Eq. (5a). Then, from $a + \delta a$, S_t can be obtained using Eq. (5b) and from $|S_t|^2$, output power can be calculated. Using this approach and assuming $\Omega_r \cos(\omega_m t + \phi_{HE}(\omega_m)) = \frac{\Omega_r}{2}\left(e^{j(\phi_{HE} + \omega_m t)} + e^{-j(\phi_{HE} + \omega_m t)}\right)$, $\hat{P}_{out}$ is found to be:

$$\hat{P}_{out} = \mu e^{j\phi_{HE}}\left[\frac{\Omega_r a_0 S_{t0}^*}{\frac{1}{\tau} + j(\Delta\omega + \omega_m)} + \frac{\Omega_r^* a_0^* S_{t0}}{\frac{1}{\tau} - j(\Delta\omega - \omega_m)}\right]. \tag{7}$$

By substituting a_0 and S_{t0} from Eq. (6) into Eq. (7) and after some manipulation, we arrive at:

$$\hat{P}_{out} = \frac{2\mu^2 P_{in} e^{j\phi_{HE}} \operatorname{Re}(\Omega_r)}{\frac{1}{\tau^2} + \Delta\omega^2}\left[\frac{j\omega_m(\tan(\phi_{\Omega_r})(\frac{1}{\tau_l} - \frac{1}{\tau_e}) - \Delta\omega) - 2\frac{\Delta\omega}{\tau_l} - \tan(\phi_{\Omega_r})(\Delta\omega^2 - \frac{1}{\tau}(\frac{1}{\tau_l} - \frac{1}{\tau_e}))}{-\omega_m^2 + \frac{2}{\tau}(j\omega_m) + \Delta\omega^2 + \frac{1}{\tau^2}}\right], \tag{8}$$

where $P_{in} = |S_i^2|$ and ϕ_{Ω_r} is the phase of Ω_r. The ring modulator transfer function, $H_t(\omega_m)$, can now be found directly from Eq. (8) by replacing Ω_r with $\hat{V}_{in} \times |H_E(\omega_m)| \times H_{EO}$ and dividing $\hat{P}_{out}$ by $\hat{V}_{in}$. Having $\tan(\Omega_r) = \tan(\phi_{HEO})$, where ϕ_{HEO} is the phase of H_{EO} in Eq. (4), $H_t(\omega_m)$ is found as:

$$H_t(\omega_m) = \frac{2\mu^2 P_{in}(-\frac{\omega_r}{n_g}\frac{\partial n_{eff}}{\partial v}|_{V_{DC}})}{\frac{1}{\tau^2} + \Delta\omega^2}\frac{(\tan(\phi_{HEO})(\frac{1}{\tau_l} - \frac{1}{\tau_e}) - \Delta\omega)}{1 + j\omega_m R_{eq}C_{eq}}\left[\frac{j\omega_m - \frac{2\frac{\Delta\omega}{\tau_l} + \tan(\phi_{HEO})(\Delta\omega^2 - \frac{1}{\tau}(\frac{1}{\tau_l} - \frac{1}{\tau_e}))}{\tan(\phi_{HEO})(\frac{1}{\tau_l} - \frac{1}{\tau_e}) - \Delta\omega}}{-\omega_m^2 + \frac{2}{\tau}(j\omega_m) + \Delta\omega^2 + \frac{1}{\tau^2}}\right]. \tag{9}$$

The transfer function in Eq. (9) can be written in s-domain ($j\omega_m \to s$) as:

$$H_t(s) = G_{DC}\frac{1}{1 + \frac{s}{\frac{1}{R_{eq}C_{eq}}}}\left[\frac{(-\frac{s}{z} + 1)\omega_n^2}{s^2 + 2\zeta\omega_n s + \omega_n^2}\right] \tag{10}$$

where $\omega_n = \sqrt{\Delta\omega^2 + \frac{1}{\tau^2}}$, $\zeta = 1/\sqrt{1 + (\tau\Delta\omega)^2}$, and the DC gain ,$G_{DC} = H_t(0)$, is:

$$G_{DC} = \frac{2\mu^2 P_{in}(\frac{\omega_r}{n_g}\frac{\partial n_{eff}}{\partial v}|_{V_{DC}})}{\omega_n^4}(2\frac{\Delta\omega}{\tau_l} + \tan(\phi_{HEO})(\Delta\omega^2 - \frac{1}{\tau}(\frac{1}{\tau_l} - \frac{1}{\tau_e}))). \tag{11}$$

Based on the small-signal transfer function of a ring modulator in Eq. (10), for non-zero detuning, ring modulator is a third-order system with a complex-conjugate pole pair, one real pole, and a real zero at the following locations:

$$p_{1,2} = -\frac{1}{\tau} \pm j\Delta\omega,$$

$$p_3 = -\frac{1}{R_{eq}C_{eq}}, \tag{12}$$

$$z = \frac{2\frac{\Delta\omega}{\tau_l} + \tan(\phi_{HEO})(\Delta\omega^2 - \frac{1}{\tau}(\frac{1}{\tau_l} - \frac{1}{\tau_e}))}{\tan(\phi_{HEO})(\frac{1}{\tau_l} - \frac{1}{\tau_e}) - \Delta\omega}.$$
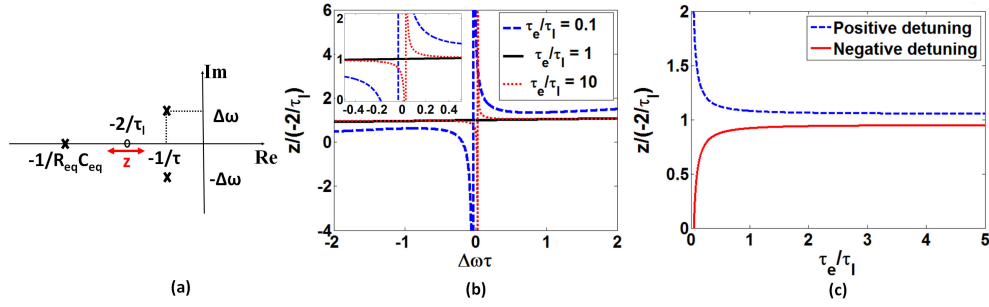
Fig. 2. (a) Pole-zero diagram of a ring modulator. Location of zero divided by $-2/\tau_l$ (b) versus $\Delta\omega\tau$, excluding $\Delta\omega\tau = 0$, for three coupling conditions (c) versus τ_e/τ_l at $\Delta\omega\tau = \pm 2$.

A pole-zero diagram of $H_t(\omega_m)$ is shown in Fig. 2(a). As illustrated in the figure, the real and imaginary parts of $p_{1,2}$ depend on the photon life time and the value of the laser detuning, respectively. However, as expected from Eq. (12), the location of the zero is more complicated. The arrow close to $-2/\tau_l$ in Fig. 2(a) indicates that the location of z is in the vicinity of $-2/\tau_l$, where the distance depends on the coupling condition and on the value/sign of the laser detuning. To make this more clear, $z/(-2/\tau_l)$ is plotted in Fig. 2(b) versus $\Delta\omega\tau$, excluding $\Delta\omega\tau = 0$, for three cases of strong over-coupled, $\tau_e = 0.1\tau_l$, critical-coupled, $\tau_e = \tau_l$, and strong under-coupled, $\tau_e = 10\tau_l$, ring modulator. The ring modulator response at $\Delta\omega = 0$ will be discussed later in the paper. The zoomed-in view is also shown in inset of Fig. 2(b). Here, we assume to have $\tau_l = 80ps$ and $\tan(\phi_{HEO}) = 0.04$. In case of both under- and over-coupled rings, because of the term in the denominator of the zero shown in Eq. (12), z approaches infinity as $\Delta\omega$ becomes equal to $\tan(\phi_{HEO})(1/\tau_l - 1/\tau_e)$. Also, as shown, in the over-coupled case, z is farther from $-2/\tau_l$ compared with the critical- and the under-coupled cases. To see the dependency of the z location on the coupling condition, z is calculated as a function of τ_e/τ_l at $\Delta\omega = \pm 2/\tau$ and plotted in Fig. 2(c). This detuning is equal to the resonator linewidth. For large detuning, $\Delta\omega >> \tan(\phi_{HEO})(1/\tau_l - 1/\tau_e)$, z can be written as:

$$z = \frac{-2}{\tau_l} - \frac{\tan(\phi_{HEO})}{\Delta\omega}(\Delta\omega^2 - \frac{1}{\tau}(\frac{1}{\tau_l} - \frac{1}{\tau_e})). \tag{13}$$

As $(1/\tau_l - 1/\tau_e)$ is negative for over coupling condition, 0 for critical coupling condition, and positive for under coupling condition, deviation of z from $-2/\tau_l$ increases by moving towards under-coupling condition. Another important point from Fig. 2(c) is that the location of zero depends on the sign of laser detuning. According to Fig. 2(c), moving from under coupling condition to deep over coupling condition leads to farther zero locations for positive and negative detuning. Consequently, from the transfer function point of view, it is clear that the frequency response of the ring modulator will be different depending on the sign of the detuning where this difference becomes more significant going towards over-coupling condition. The different frequency response for positive and negative detunings was expected based on the asymmetric side-band generation [10].

It can also be seen from Eq. (9) and (10) that when $\Delta\omega = 0$, $H_t(s)$ becomes:

$$H_t(s)|_{\Delta\omega=0} = \frac{-2\mu^2 P_{in}(\frac{\omega_r}{n_g}\frac{\partial n_{eff}}{\partial v}|_{V_{DC}})}{\frac{1}{\tau^3}} \frac{\tan(\phi_{HEO})(\frac{1}{\tau_l} - \frac{1}{\tau_e})}{1 + \frac{s}{\frac{1}{R_{eq}C_{eq}}}} \frac{1}{1 + \frac{s}{\frac{1}{\tau}}}, \tag{14}$$
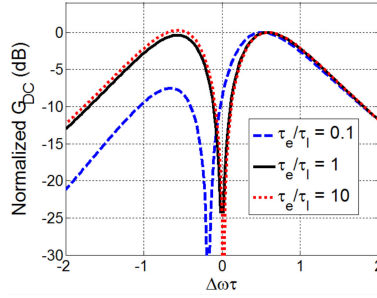
Fig. 3. DC gain for three coupling conditions versus $\Delta\omega\tau$.

which is a second order system with two real poles at $-1/R_{eq}C_{eq}$ and $-1/\tau$ when $\tau_l \neq \tau_e$.

Normalized absolute value of DC gain (Eq. 11) is plotted versus $\Delta\omega\tau$ in Fig. 3 for three aforementioned coupling conditions when $\tau_l = 80$ps and $\tan(\phi_{HEO}) = 0.04$. Based on this figure, the DC gain becomes very small for detunings close to zero. However, as shown in Fig. 3, when $\tau_e \neq \tau_l$, G_{DC} minimum shifts from $\Delta\omega = 0$ to positive and negative detunings for under- and over-coupled cases, respectively. The DC gain minimum shift is larger for the over-coupled case compared with the under-coupled case. According to Fig. 3 and Eq. (11), in contrary to what was reported in [9], only for critically-coupled ring modulator, $\tau_l = \tau_e$, the small-signal modulation is zero at $\Delta\omega = 0$. The fact that $\tan(\phi_{HEO})$ is non-zero in Eq. (11), due to the loss modulation accompanying the index modulation, results in a non-zero small-signal modulation at zero detuning for over- and under-coupled rings. Also, this results in the coupling-condition dependent G_{DC} maximum locations, as can be seen from Fig. 3.

3. Verification of the small-signal model

To verify the closed-form small-signal transfer function in the previous section, we characterize an all-pass ring modulator fabricated in IME A*Star process [21]. The cross section of the ring modulator waveguide in the high speed section and an optical microscope image of the fabricated device are shown in Figs. 4(a) and 4(b), respectively. The device is implemented on a 220nm Si on a 2μm buried oxide layer. The nominal doping concentration for low doped region inside the waveguide is $3 \times 10^{17} cm^{-3}$ for n and $5 \times 10^{17} cm^{-3}$ for p, and for high-doped region is $10^{20} cm^{-3}$. The pn junction is positioned with 50nm offset with regards to the waveguide center. The lateral pn junction is taking 75% of the ring circumference and is not covering the coupling region. Radius of the ring is 10μm, waveguide width is 500nm, and gap between the ring and the bus waveguide is 350nm. Transmission spectra at through ports of the ring modulator are shown in Fig. 5(a) under reverse bias voltages of 0.5, 0 , -0.5,-1, and -2V applied to the RF pads. Optical power loss, $\alpha(V)$, and through coupling coefficient, t, are extracted from the measured spectra at various bias voltages based on the method presented in [22]. Figure 5(b) shows the extracted $\Delta\alpha$ in dB/cm versus voltage. From the extracted coupling coefficient and the voltage-dependent power loss coefficient in $1/m$, τ_l and τ_e are calculated [20]:

$$\tau_l = \frac{2}{v_g \alpha(v)},$$
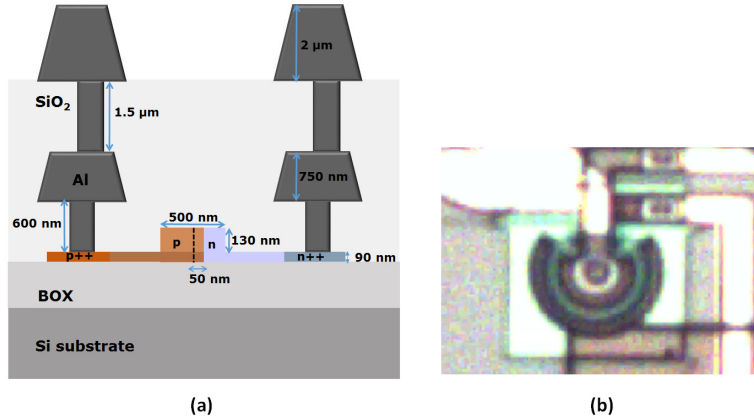$$\tau_e = \frac{2L_{rt}}{v_g \kappa^2},$$
(15)

Fig. 4. (a) Cross section of the ring modulator waveguide in the active region. (b) Optical microscope image of the fabricated ring modulator.

where v_g is the group velocity, κ is the cross coupling coefficient ($\sqrt{1-t^2}$), and L_{rt} is the round-trip length. Also, n_g, was extracted to be ≈ 3.9. As the coupling region in the ring is not pn-doped, the change in τ_e by varying voltage is insignificant.

From Eq. (15), τ_l is calculated as a function of voltage and is fitted to a cubic polynomial. τ_l and τ_e are found to be 82.2ps and 65.3ps, respectively, at $V_{DC} = 1.5V$. Having $\tau_e < \tau_l$ shows that the ring is over-coupled as it was expected from notch depth-bias voltage dependency in Fig. 5(a). Also, $\frac{\partial(1/\tau)}{\partial v}|_{V_{DC}}$ is calculated to be -2.7×10^8 $1/s/V$. Moreover, extracted n_{eff} as a function of voltage is plotted in Fig. 5(c) together with the fitted quadratic curve with Eq shown in the figure. From this, $\frac{\partial n_{eff}}{\partial v}|_{V_{DC}}$ is calculated to be 2.35×10^{-5} $1/V$. Quality factor of the ring is about 22,200 at V_{DC}. In the small-signal circuit model, R_{in} is taken to be 50Ω,
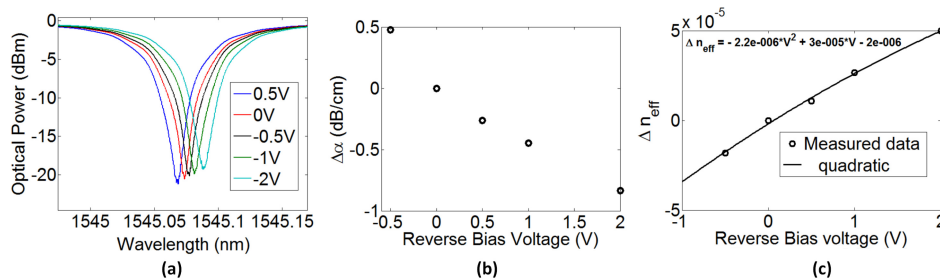

Fig. 5. (a) Measured optical power transmission spectra (resolution of $2.5 \times 10^{-4} nm$) at various bias voltages . Extracted (b) $\Delta \alpha$ and (c) Δn_{eff} from the measured spectra shown in (a).

and C_j and R_j are calculated based on the methods presented in [16] to be 11fF and 160Ω. The calculated value for C_j closely matches the measured junction capacitance in [23] which is fabricated in the same foundry and has the same waveguide doping and geometry as here. The R_j is also calculated based on the measured sheet resistance in [23]. Other circuit elements (C_{pad}, R_{Si}, and C_{ox}) which are less important are assumed to be the same as [15] which has similar waveguide cross section and metal. Based on these values, the electrical bandwidth of the ring modulator, $f_{RC} = 1/2\pi R_{eq} C_{eq}$, is found to be 61.5GHz which is around $7\times$ higher than

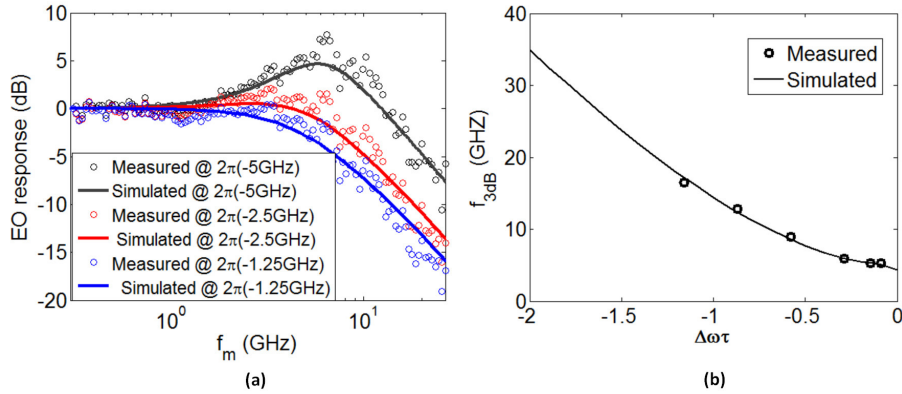the optical bandwidth of $f_Q = 8.7 GHz$ for this measured device.

Fig. 6. Measured and simulated small-signal (a) electro-optical response versus modulation frequency, f_m, (b) 3dB bandwidth of the reverse-biased ring modulator.

Substituting these parameters in Eq. (9), we simulated the electro-optical response of the ring modulator at various laser detunings. The results for three laser detunings of $2\pi(-1.25GHz)$, $2\pi(-2.5GHz)$, and $2\pi(-5GHz)$ are shown in Fig. 6(a). Frequency response of the ring modulator is also measured using a 40Gbps InP waveguide photodetector and a transimpedance amplifier (TIA) photoreceiver referenced to a vector network analyzer (VNA) output. The measurement results are also shown in Fig. 6(a) in circles which shows that our model is in excellent agreement with the measurement results. All the curves are normalized with respect to their DC values (200MHz). Figure 6(a) clearly illustrates the detuning-dependent frequency response of the ring modulator. The observed peak in the frequency response occurs due to the constructive interference between the frequency detuned through-coupled input laser and the cross coupled light preexisting inside ring resonator and oscillating at its natural frequency [9–11]. Also, 3dB bandwidth, f_{3dB}, calculated from our small-signal model is plotted in Fig. 6(b) together with the measured f_{3dB} at several detunings (circles). As shown in [9–11,14], by increasing laser detuning, the device bandwidth increases due to the aforementioned peaking effect.

Due to their compact nature, any small changes in the ring modulators may lead to vast changes in the device performance. Cross wafer characterization of the silicon photonics components including ring modulator fabricated in this technology were studied earlier [24]. For every tested device, the required parameters for the frequency response modeling need to be extracted from DC measurements. We have tested the developed model at multiple design variations to confirm the model accuracy by way of comparing it to experimental results. However, for the sake of consistency and brevity of the current manuscript, such results will be presented elsewhere.

4. Gain-bandwidth product as a figure of merit

The small-signal transfer function of the ring modulator in Eq. (9) can be further simplified by neglecting the loss modulation, as for a typical SOI process we have $\frac{Im(\Omega_r)}{Re(\Omega_r)} << 1$ [10]. Based

on this assumption, the transfer function in the s-domain can be written as:

$$H_t(s) = G_{DC} \frac{1}{1 + \frac{s}{\frac{1}{R_{eq}C_{eq}}}} \left[\frac{(\frac{s}{2}+1)\omega_n^2}{s^2 + 2\zeta\omega_n s + \omega_n^2} \right], \tag{16}$$

where G_{DC} becomes:

$$G_{DC} = \frac{2\mu^2 P_{in}(\frac{\omega_r}{n_g}\frac{\partial n_{eff}}{\partial v}|_{V_{DC}})\Delta\omega}{(\Delta\omega^2 + \frac{1}{\tau^2})^2} \frac{2}{\tau_l}. \tag{17}$$

The laser detuning which maximizes the DC gain can be calculated by setting $\frac{\partial G_{DC}}{\partial\Delta\omega} = 0$. Based on this, at $\Delta\omega = 1/(\sqrt{3}\tau)$, DC gain is maximized. This is similar to what was shown in [9,10]. Also, it can be seen from Eq. (17) that at critical coupling ($\tau_e = \tau_l$) and for a constant $\Delta\omega\tau$, G_{DC} is proportional to τ^2. This can be qualitatively justified as follows: at the same $\Delta\omega\tau$, a transmission spectrum of the ring with higher quality factor, or τ, has higher slope, and consequently higher G_{DC}.

The ring 3dB bandwidth can be calculated by setting $|H(\omega_m)|$ equal to $G_{DC}/\sqrt{2}$ in Eq. (16). In the case when $1/R_{eq}C_{eq} >> 1/\tau$ and at critical coupling, f_{3dB} is calculated to be:

$$f_{3dB} = \frac{1}{2\pi\tau} \sqrt{3\Delta\omega^2\tau^2 + \Delta\omega^4\tau^4 + \sqrt{1 + 2\Delta\omega^2\tau^2 + 10\Delta\omega^4\tau^4 + 6\Delta\omega^6\tau^6 + \Delta\omega^8\tau^8}}. \tag{18}$$

According to Eq. 18, for a constant $\Delta\omega\tau$, f_{3dB} is proportional to $1/\tau$ and consequently f_Q, given that $f_Q = 1/\pi\tau$. This comes from the earlier assumption of $1/R_{eq}C_{eq} >> 1/\tau$ which neglects the bandwidth limitation arises from f_{RC}. For the special case of $\Delta\omega\tau = 1$, which represents a detuning equal to the half of the resonator linewidth, f_{3dB} will be around $1.4 \times f_Q$.

Here, we use the gain-bandwidth product, $GBW = G_{DC} \times f_{3dB}$, as a FOM. For the simplified case considered here, GBW is calculated from Eq. 17 and 18 to be:

$$GBW = K\tau \frac{\Delta\omega\tau}{(\Delta\omega^2\tau^2 + 1)^2} \sqrt{3\Delta\omega^2\tau^2 + \Delta\omega^4\tau^4 + \sqrt{1 + 2\Delta\omega^2\tau^2 + 10\Delta\omega^4\tau^4 + 6\Delta\omega^6\tau^6 + \Delta\omega^8\tau^8}}$$

$$\tag{19}$$

where $K = 2\mu^2 P_{in} \frac{\omega_r}{\pi n_g} \frac{\partial n_{eff}}{\partial v}|_{V_{DC}}$. Also, as expected from G_{DC} and f_{3dB} formulas, GBW is proportional to τ. Hence, at the same $\Delta\omega\tau$, the critically coupled ring with higher quality factor has higher GBW.

In order to see the effect of detuning on DC gain, bandwidth, and GBW, $\Delta\omega$ is swept while the rest of the parameters are kept constant. Normalized G_{DC}, f_{3dB}, and GBW are plotted in Fig. 7 versus $\Delta\omega\tau$. In this figure, only positive detunings are shown as the plots are symmetric around $\Delta\omega = 0$ due to the no loss modulation assumption. According to Fig. 7 top, increasing $\Delta\omega$ beyond $1/(\sqrt{3}\tau)$ to increase the bandwidth introduces a trade-off between G_{DC} and f_{3dB} as was observed previously in [9, 12]. Figure 7 bottom shows that the product of G_{DC} and f_{3dB} (FOM) reaches its maximum value when $\Delta\omega = 1.129/\tau$.

The closed-form GBW formula (Eq. (19)) for the simplified case helps develop an understanding of the ring modulator small signal behavior. However, obtaining such a formula with loss modulation, electrical bandwidth limitation, and for other coupling conditions is more complicated. Therefore, in the following section, we will study GBW numerically using Eq. (10) as a means to study the ring modulator frequency response.
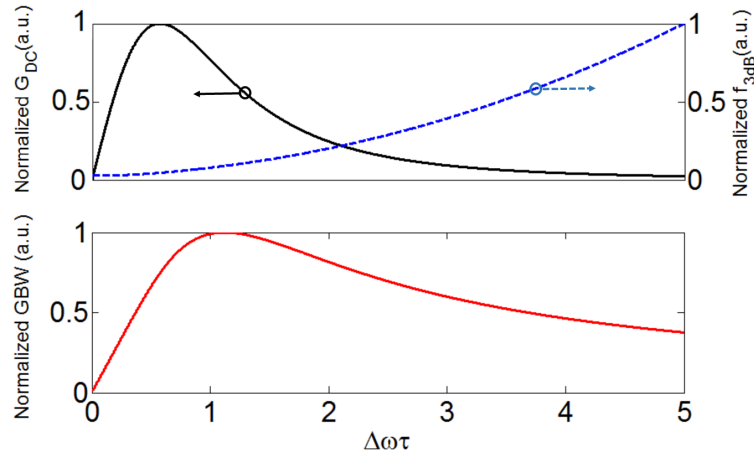
Fig. 7. Normalized G_{DC}, f_{3dB}, and GBW versus $\Delta\omega\tau$ for a constant τ.

5. Effect of pole/zero locations on ring modulator gain-bandwidth product

We now study the effect of the ring modulator electrical behavior on GBW based on the small-signal transfer function. This is examined by sweeping $R_{eq}C_{eq}$ in Eq. (10), so that f_{RC} be equal to $m \times f_Q$, m an integer value. The pole-zero diagram is shown in Fig. 8(a) where locations of the poles/zero are indicated based on f_Q and f_{RC} when $\tau_l = \tau_e = 80$ps. Figure 8(b) shows GBW for several f_{RC} values versus $\Delta\omega\tau$. It is clearly shown that increasing f_{RC} will result in increasing GBW. However, the rate saturates as f_{RC} increases above a certain value. To observe this effect more clearly, maximum GBW for both positive and negative detunings are plotted versus f_{RC}/f_Q in Fig. 8(c). The plots show that up to $f_{RC}/f_Q = 3$ both curves initially rise rapidly but then the rate decreases beyond this value and almost saturates at $f_{RC}/f_Q > 11$. This occurs as for such large values of f_{RC}, p_3 is far apart from $p_{1,2}$ and z, and therefore, its effect becomes almost insignificant. Figure 8(d) shows the plot of $(\Delta\omega\tau)_{max}$ corresponding to the GBW maximums for both positive and negative detunings versus f_{RC}/f_Q. According to this figure, $(\Delta\omega\tau)_{max}$ also varies depending on p_3 location. For large f_{RC} ($f_{RC}/f_Q = 100$), $(\Delta\omega\tau)_{max}$ becomes 1.134 for positive and 1.119 for negative detunings. These values are slightly different from the predicted value of 1.129 obtained from Fig. 7 (bottom), as we had neglected the loss modulation in obtaining the simplified GBW in Eq. (19).

It is well known that there is a trade off between bandwidth and DC gain (e.g. see Fig. 7). The amount of penalty in DC gain caused by varying the laser detuning is defined as G_{DC} divided by its maximum value achieved among all the detunings [9]. It is shown in [9] that increasing f_{RC} increases the trade-off efficiency between bandwidth and DC gain penalty. To study this further, f_{3dB}/f_Q versus G_{DC} penalty is plotted in Fig. 9(a). This figure shows the predicted increase in trade-off efficiency, however, there is a saturation point beyond which, trade-off efficiency does not increase significantly. To make this more clear, slopes of these curves, obtained by fitting a line to each, are calculated and plotted in Fig. 9(b) as a trade off coefficient versus f_{RC}/f_Q for both positive and negative detunings. As shown, the saturation point of $f_{RC}/f_Q \approx 11$, observed in Fig. 8(c), is also clearly observable here. Also, according to Fig. 9(b), positive detuning, in this case of the critical coupling, reaches higher trade off coefficient compared with the negative detunings. Although here we assumed critical coupling condition, the result is the same for over- and under-coupling (e.g. in [9] the ring modulator was assumed to be under-coupled).
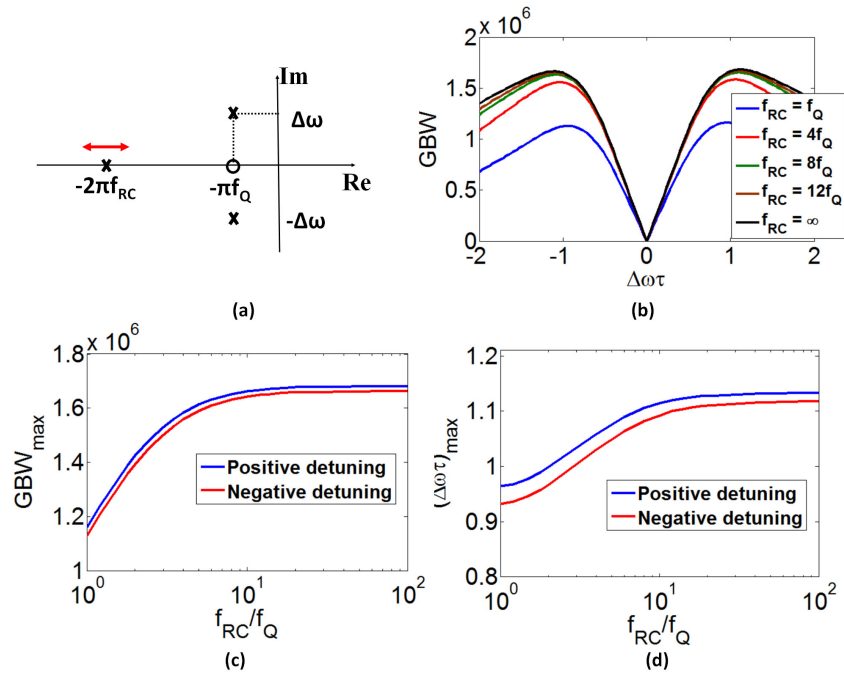
Fig. 8. (a) Pole-zero diagram of a ring modulator. Simulated (b) GBW versus $\Delta\omega\tau$ for several f_{RC} (c) GBW maxima versus f_{RC}/f_Q (d) $\Delta\omega\tau$ corresponding to the GBW maxima versus f_{RC}/f_Q.

Here, we assumed that the variation of the ring modulator electrical bandwidth (p_3 location) does not affect the other poles and zero locations. However, improvement of f_{RC} may come at the cost of excess optical loss which leads to variation of the entire pole-zero diagram. Therefore, depending on the selected f_{RC} improvement method, variation of $p_{1,2}$ and z may need to be taken into account.
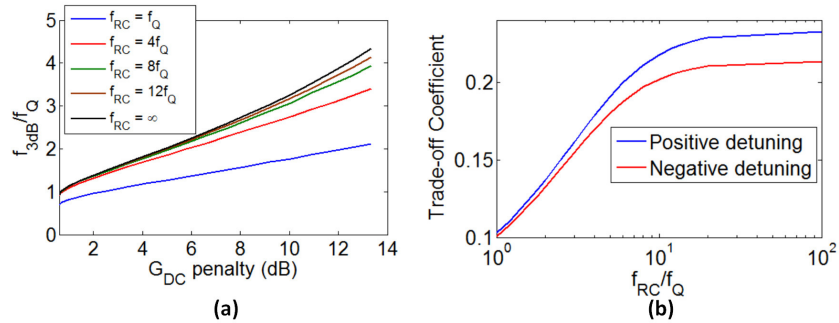

Fig. 9. (a) Simulated f_{3dB}/f_Q versus DC gain penalty for several f_{RC}. (b) Trade-off coefficient, defined as the slope of the lines fitted to f_{3dB}/f_Q versus DC gain penalty curves, versus f_{RC}/f_Q for both positive and negative detunings.

Next, we study the effect of coupling condition on the ring modulator frequency response. This is done by varying τ_e and keeping τ_l constant. This can be translated to various p_1 and p_2

locations with regards to z. First, we consider three cases of $\tau_e = \tau_l/2$ (over-coupled), $\tau_e = \tau_l$ (critical-coupled), and $\tau_e = 2\tau_l$ (under-coupled) as shown in Fig. 10(a). For simplicity, the locations of z are shown to be at $-2/\tau_l$ and insensitive to the coupling condition as for this range of τ_e/τ_l the walk-off is small (Fig. 2(c)). Here, it is assumed that $f_{RC} = 12 \times f_Q$ and $\tau_l = 80$ps for three cases studied here. As such, p_3 is equal to $-24/\tau$ as shown in Fig. 10(a), and from left to right we have $|\text{Re}(p_{1,2})| > |z|$, $|\text{Re}(p_{1,2})| = |z|$, $|\text{Re}(p_{1,2})| < |z|$, respectively. Figure 10(b) shows Bode plots of each case presented in Fig. 10(a), ignoring the third pole as it is located far from other poles and zero. It is well known that when there is no resonant peaking, Bode plot describes frequency response of a system with a pair of complex-conjugate poles more accurately. This requires $\zeta > 0.707$ and therefore $|\Delta\omega\tau| < 1$. In this regime, it is easier to qualitatively describe the frequency response and compare the three aforementioned cases. Also, considering the poles/zero configurations in Fig. 10(a) and given that τ_l is the same in the three examples, it is clear that $\omega_{n1} > \omega_{n2} > \omega_{n3}$ for the same $\Delta\omega$. Here, indices 1, 2, and 3 are corresponding to over-, critical-, and under-coupled cases. According to Fig. 10(b), in the case of $\tau_e = \tau_l/2$ where $z < \omega_{n1}$, as the input frequency approaches z, the frequency response magnitude starts increasing at a rate of 20dB/dec until ω_{n1} where the frequency response amplitude start falling at a rate of -20dB/dec. For $\tau_e = \tau_l$ where $z = \omega_{n2}$, the magnitude rolls-off at the rate of -20dB/dec at input frequency equal to z and onward. When $\tau_e = 2\tau_l$, i.e. $z > \omega_{n3}$, the magnitude rolls off at a rate of -40dB/dec at ω_{n3} until input frequency reaches z after which the rate becomes -20dB/dec. Consequently, it is clear from Bode plots in Fig. 10(b) that f_{3dB} is higher for $\tau_e = \tau_l/2$ compared with the other two cases.
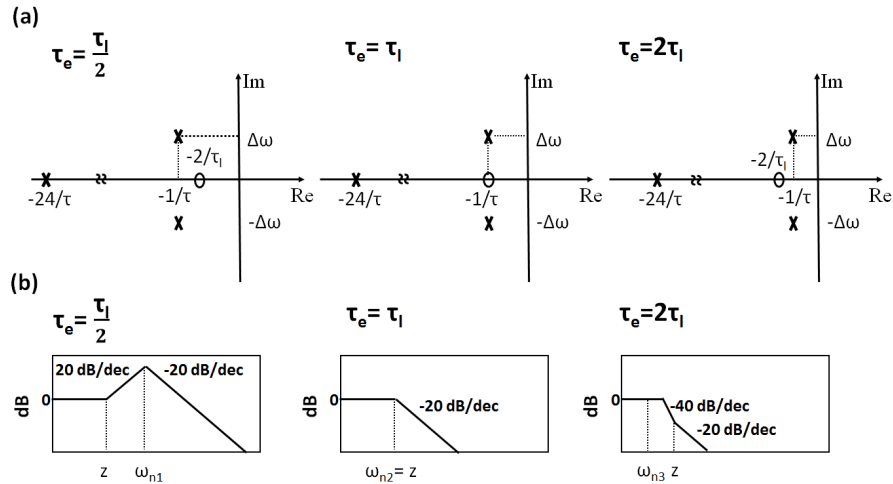

Fig. 10. (a) Pole-zero diagrams of the ring modulator when $p_3 = -24/\tau$ and from left to right $\tau_e = \tau_l/2$, $\tau_e = \tau_l$, and $\tau_e = 2\tau_l$. (b) corresponding Bode plots of the pole-zero diagrams shown in (a).

Breaking the assumption of $\zeta > 0.707$ and sweeping $\Delta\omega$, f_{3dB} of the ring modulators with zero-pole diagrams shown in Fig. 10(a) are calculated from our model and are plotted in Fig. 11(a). As shown, the prediction based on the Bode plots in Fig. 10(b) is also valid when $\zeta < 0.707$. This figure also shows that the rate of change in f_{3dB} as a function of $|\Delta\omega|$ is higher for $\tau_e = \tau_l/2$ than $\tau_e = \tau_l$ and $\tau_e = 2\tau_l$. It has been shown that moving toward under coupling condition results in increasing DC gain [9]. However, GBW plots versus $\Delta\omega\tau$ shown in Fig. 11(b) suggest that GBW is higher for over-coupled ring than both critical- and under-coupled rings. Also, according to Fig. 11(b), contrary to the assumption made in [17],

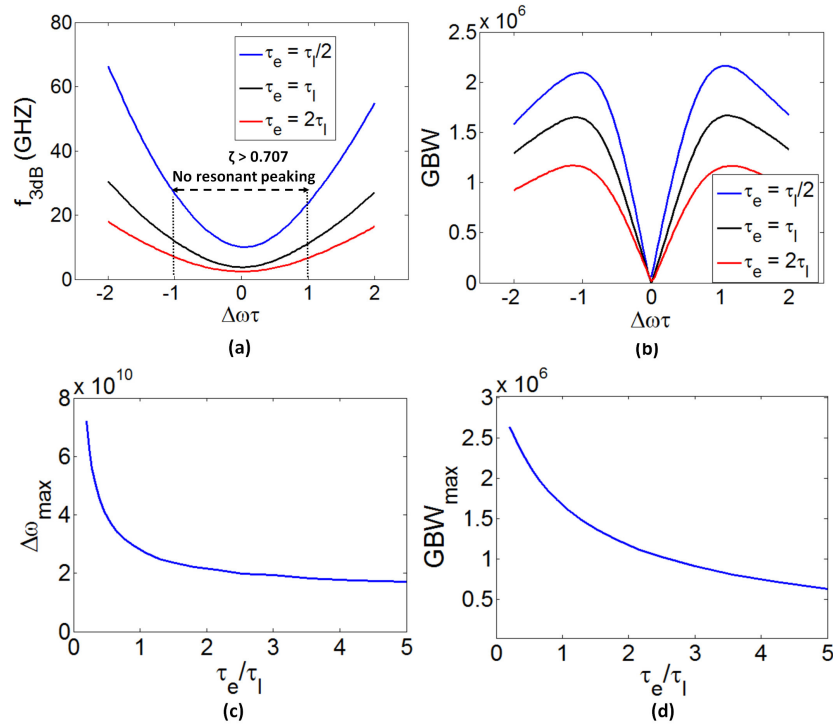the location of peak is also shifting by changing the coupling condition.

Fig. 11. (a) Ring modulator 3dB bandwidth (b) GBW versus $\Delta\omega\tau$ when $\tau_l = 80ps$ and τ_e is equal to $\tau_l/2$, τ_l, and $2\tau_l$. (c) Laser detunings corresponding to the maximum GBW at positive detunings (d) GBW maximum versus τ_e/τ_l for $\tau_l = 80ps$.

This is further investigated by sweeping τ_e/τ_l and simulating GBW. The τ_e/τ_l range is taken to start from 0.3 to make sure the location of zero stays close to $-2/\tau_l$ (Fig. 10(c)) as our focus here is to study the location variation of the complex-conjugate pole pair only. The optimum laser detuning corresponding to the GBW maximum at positive detunings is plotted versus τ_e/τ_l which shows that moving from under- to over-coupling condition results in decreasing optimum laser detuning. The GBW at this optimum detuning is illustrated in Fig. 11(d). The figure suggests a monotonous decay in *GBW max* in the selected range of τ_e/τ_l, as poles move toward z and closer to the imaginary axis. Consequently, higher GBW is achievable for over-coupled ring modulator.

Although GBW is a metric for the small signal frequency response of the ring modulator, other performance metrics should also be considered when choosing the laser detuning. For example, extinction ratio and insertion loss are also dependent on the laser detuning. Despite the high GBW for deep over-coupled ring modulator, the maximum achievable extinction ratio decreases significantly which is not desirable for various applications.

6. Conclusion

In this paper, a closed-form formula was presented for the ring modulator small-signal response. The derived model was verified using experimental results for a sample ring modulator. From this small-signal transfer function, the locations of three poles and a zero were obtained. The locations of poles and zero were shown to vary with the parameters such as electrical band-

width, coupling condition, optical loss, sign/value of laser detunings. The response of the ring modulator and the defined FOM variation over several pole-zero diagrams were simulated and discussed. Developing such a closed-form transfer function allowed us to analyze the ring modulator small-signal behavior based on pole-zero locations. Through this approach, it was shown that over-coupled ring modulators can be generally more favorable as they provide better GBW product.

Acknowledgment